Nanofluidic ion-exchange membranes

Can their conductance compete with polymeric ion-exchange membranes?

Petrov, Kostadin V.; Hurkmans, Jan Willem; Hartkamp, Remco; Vermaas, David A.

DOI
10.1016/j.memsci.2024.123238

Publication date
2024

Document Version
Final published version

Published in
Journal of Membrane Science

Citation (APA)
Petrov, K. V., Hurkmans, J. W., Hartkamp, R., & Vermaas, D. A. (2024). Nanofluidic ion-exchange membranes: Can their conductance compete with polymeric ion-exchange membranes? *Journal of Membrane Science*, *712*, Article 123238. https://doi.org/10.1016/j.memsci.2024.123238

Journal of Membrane Science 712 (2024) 123238

Contents lists available at ScienceDirect

Journal of Membrane Science

journal homepage: www.elsevier.com/locate/memsci

Nanofluidic ion-exchange membranes: Can their conductance compete with polymeric ion-exchange membranes?

Kostadin V. Petrov [a], Jan-Willem Hurkmans [a], Remco Hartkamp [b], David A. Vermaas [a,*]

[a] Department of Chemical Engineering, Delft University of Technology, 2629 HZ Delft, the Netherlands
[b] Process & Energy Department, Delft University of Technology, 2628 CB Delft, the Netherlands

A B S T R A C T

Nanofluidic membranes (NFMs) are gaining prominence as alternative ion-exchange membranes, because of their distinct selectivity mechanism, which does not rely on functional groups on a polymeric backbone but rather on charged nanopores that allow straight ion-conductive pathways for efficient ion transport. We measured the conductivity of commercial anodized aluminum oxide membranes with different pore sizes under different current densities and electrolyte concentrations. We also simulated a nanopore channel with charged walls between two electrolyte reservoirs. Our findings indicate that electrolyte concentration is the main parameter that determines NFM conductivity, with a linear dependence at least up to 1 M. Our study shows that the optimal pore length is between 0.5 and 5 μm considering the trade-off between selectivity and conductance. On the other hand, the conductance is not sensitive to the pore diameter. Conical nanopores are a way to increase conductance, but according to our results, this increase comes at the expense of selectivity. Our findings suggest that NFMs can outperform polymeric ion-exchange membranes in certain electrochemical applications, such as reverse electrodialysis, but not in applications that use low electrolyte concentrations on both sides of the membrane.

1. Introduction

With the pressing need to reduce our reliance on fossil fuels and mitigate the environmental impact of traditional industrial processes, electrochemical membrane technologies have taken center stage in addressing these multifaceted challenges [1–3]. Ion-exchange membranes (IEMs), are a key component for technologies such as the chlor-alkali process [4], fuel cells [5], electrodialysis and redox-flow batteries [6,7], due to their ability to selectively transport ions.

IEMs are usually thin films (~100 μm) of a polymeric backbone structure with charged functional groups, which are responsible for the ion-selectivity [8,9]. These polymeric materials offer several advantages, including flexibility, cost-effectiveness, and ease of fabrication. However, they do present certain intrinsic issues, such as swelling of the backbone structure, which leads to a limited charge density and a trade-off between conductivity and selectivity [10,11]. Most IEMs have a fixed charge density of 0.5–3 M, which limits their selectivity, especially at high electrolyte concentrations [12]. Additionally, the interstitial space within the dense polymeric structure where ion transport takes place are often comparable in size to the ions themselves (Fig. 1a). As a result, tortuosity and electrostatic effects cause a high resistance to ion transport in polymeric IEMs [13–15]. These drawbacks hinder the scale-up possibilities of technologies such as reverse electrodialysis (RED), redox flow batteries, and CO_2 electrolysis [16–20].

Nanofluidic membranes (NFMs) have recently gained attention as an alternative to polymeric IEMs [13,21]. They are made from inorganic materials, with nanopores typically between 1 and 20 nm in size. Since this size is of the same order of magnitude as the electrical double layer thickness, the fluid will have a non-zero charge density throughout the pore due to double layer overlap [22]. This overlap causes an increased (Donnan) potential within the pore, which is responsible for rejecting co-ions (ions with the same charge as the pore surface) and allowing counter-ions (oppositely charged) to permeate [23]. Because of their inorganic nature, NFMs do not suffer from the swelling issues that IEMs have. The pores in NFMs are much larger than the ion size, which promotes ion transport, and the ionic pathway can be optimized to increase ionic conductivity [13]. Existing work on NFMs includes graphene nanopores, boron nitride nanotubes and metal oxide nanopore arrays. Work on single nanotubes or single nanopores has demonstrated promise for obtaining high selectivity and high throughput [24–26], but fabrication is still limited to a small number of pores per sample. Therefore, we focus on metal oxide nanopore arrays, which are commercially available with dense arrays and pore sizes between 10 and 100 nm.

Previous work has shown that NFMs can achieve a good ion-selectivity, if optimized [27–30]. However, little is known about what

* Corresponding author.
E-mail address: D.A.Vermaas@tudelft.nl (D.A. Vermaas).

https://doi.org/10.1016/j.memsci.2024.123238
Received 24 May 2024; Received in revised form 20 August 2024; Accepted 21 August 2024
Available online 22 August 2024

parameters enhance their conductivity. Nanofluidics literature often uses single nanochannels showing ionic resistances in the kΩ.cm^2 range, which is too high to be applied in practical electrochemical applications. NFMs have seen development, mostly for power generation through RED, which has slightly decreased their ionic resistance [31,32]. Graphene oxide (GO) membranes are an example of a material that has recently been developed to exhibit ionic resistance as low as 3.9 Ω cm^2 [30]. However, GO membranes are made of stacked 2D sheets, which leads to a non-optimal and tortuous ionic pathway (Fig. 1b) and makes it harder to optimize the trade-off between selectivity and conductance. Cylindrical nanopores that directly connect one side of the membrane to the other have promise to further reduce ionic resistance, since this geometry allows the ions to travel the shortest path (Fig. 1c) [13].

In this work, we study the conductivity of nanofluidic membranes under different operational parameters, such as current density and electrolyte concentration. We use anodized aluminum oxide (AAO) membranes with different pore sizes and a Poisson-Nernst-Planck model to better understand the conductivity of nanofluidic membranes. AAO is a commercial material with a dense array of cylindrical nanopores, which make it an ideal model material to study NFMs. We examine and discuss their potential for practical applications.

2. Methods

2.1. Experimental methods

This section describes the measurements of the ionic resistance of AAO membrane discs with a diameter of 1.3 ± 0.1 cm, a thickness of 50 μm, and an array of cylindrical nanopores with different pore sizes (InRedox, Colorado, USA), in different KCl concentrations. The membranes act as an anion-exchange membrane (AEM) at neutral pH, and their detailed characterization can be found in our previous work [27]. We found that these membranes have a low effective porosity due to the non-uniform size and convergence and divergence of numerous nanochannels along their length, resulting in dead-end pores and a lack of direct connection between the two sides of the membrane. Additionally, our characterization of the AAO membranes revealed a wider pore size distribution than provided by the supplier, with the effective pore size being 8 nm for the samples labeled as 10 nm.

The ionic resistance was measured in a 6-compartment, 4-electrode setup, as illustrated in Fig. 2a. In this setup, two platinum-coated titanium electrodes were used to apply a current over the whole setup (in compartments 1 and 6), and two double-junction Ag/AgCl electrodes were connected to Luggin capillaries, placed very close (<0.5 mm) to the membrane. The latter electrodes allowed the measurement of membrane potential, which was corrected by a blank measurement, without a membrane, after every experiment. Each compartment has a volume of ~130 mL and the electrolyte within was kept flowing at 40 mL/min to mitigate concentration polarization. 0.1 M K_2SO_4 was flowed in compartments 1 and 6 to avoid any undesired Faradaic reactions – only the hydrogen and oxygen evolution reactions occurred. Since these reactions produce OH^- and H^+, respectively, a buffer solution (0.1 M K_2PO_4) was flowed in compartments 2 and 5. In compartments 3 and 4, KCl solutions were circulated, and the respective concentrations are stated along with the results. The AAO membranes were placed in a holder with 0.64 cm^2 of open area, between two flat O-rings. Cation-exchange membranes were placed between the remaining compartments, since the cation is the same in the whole setup, and anion cross-over should be avoided. Current was applied and the voltage was measured using an Autolab PGSTAT 128 N potentiostat (Metrohm, Switzerland).

Since the resistance was dependent on the applied current, it was measured using the current interrupt method [33]. A constant current was applied for 300 s, to observe a stable voltage, and then it was set to 0. The immediate voltage drop corresponds to the ohmic resistance. The resistance value was then simply calculated by Ohm's law, using the difference between average voltage of the last 30–60 s and the voltage value right after interrupt (very close to 0), and the applied current. Positive currents were measured first, followed by a re-equilibration time of at least 2 h with the electrolyte solutions, after which the negative currents were measured.

2.2. Simulations

This section describes the modeling methods, governing equations, and assumptions used to implement the space-charge model, used to describe ionic transport through a cylindrical nanopore. The modeled geometry consists of two electrolyte compartments separated by a single nanopore, as shown in Fig. 2b.

The system is modeled as a continuum system with the Poisson-Nernst-Planck (PNP) theory coupled to the Navier-Stokes equation. The model has been implemented in COMSOL Multiphysics 5.6. This PNP-based numerical model offers advantages above e.g. Teorell-Meyer-Sievers theory for ion exchange membranes [34], such as including non-cylindrical pores, water transport and concentration polarization.

Through assumption of a dilute electrolyte, the transport of dissolved species is modeled through the steady-state Nernst-Planck equation:

$$\nabla \cdot \left(- D_i \nabla c_i - D_i \frac{z_i e}{k_B T} c_i \nabla \phi + c_i \boldsymbol{u} \right) = 0 \tag{1}$$

Whereby D_i is the diffusion coefficient, c_i the concentration and z_i the valence of species i, k_B is Boltzmann's constant, e is the elementary charge, T is the temperature, ϕ is the electrolytic potential and $\boldsymbol{u}$ is the

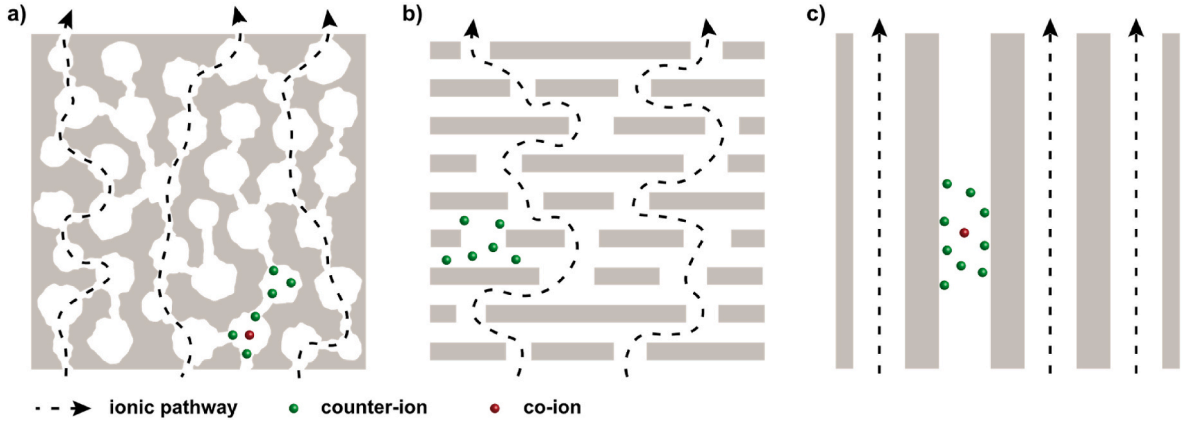

Fig. 1. – Schematic illustration of ion transport through the cross-section of a) polymeric IEMs, according to the microheterogeneous model [15], b) GO membranes and c) NFMs with cylindrical nanopores. The membrane structure is in grey, and the edges are charged surfaces.

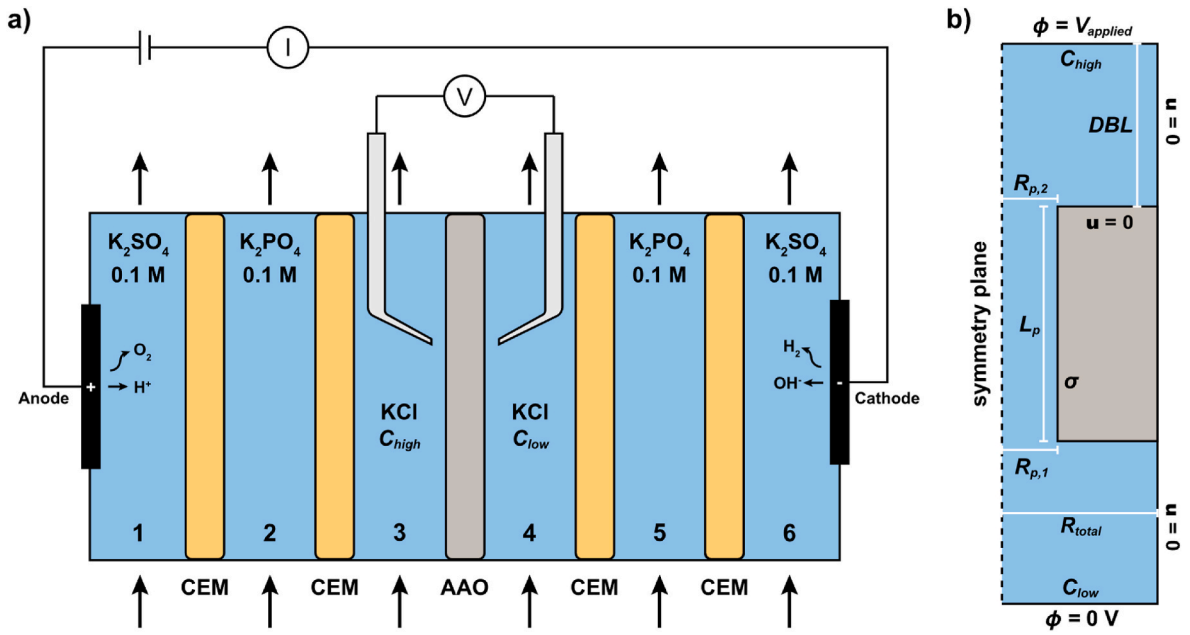

Fig. 2. – a) Schematic illustration of the 6-compartment setup used for electrical resistance measurements, b) geometry modeled in COMSOL Multiphysics.

velocity field. The electrostatic potential ϕ is resolved through the Poisson equation:

$$-\varepsilon\varepsilon_0\nabla^2\phi = \rho_e \tag{2}$$

Here, ε is the relative permittivity, ε_0 is the vacuum permittivity and ρ_e is the charge density of the solution, defined as $\rho_e = c_{K^+} - c_{Cl^-}$ for the binary system under investigation. We assume a constant relative permittivity, which we deem acceptable for nanopore diameters in the order of 10 nm. For sub-nm pores, and for low ion concentrations, the relative permittivity is no longer constant [35,36]. The velocity field is simulated through the Navier-Stokes equations for an incompressible Newtonian fluid which has been reduced to the steady-state Stokes equation since inertial effects on the length scales of a single nanopore are near zero. A Coulombic body force is added to account for electro-osmotic flow:

$$\mu\nabla^2\boldsymbol{u} - \nabla p + \rho_e\boldsymbol{E} = 0 \tag{3}$$

Here, μ is the dynamic viscosity, p is the pressure and $\boldsymbol{E}$ is the electric field, which can be expressed as $-\nabla\phi$. Conservation of mass is ensured through the continuity equation:

$$\nabla\cdot\boldsymbol{u} = 0 \tag{4}$$

The axisymmetric computational domain (Fig. 2b) consists of two reservoirs containing KCl electrolyte, separated by a nanopore of length L_p. The nanopore can be varied between a cylindrical pore with radius R_p ($R_{p,1} = R_{p,2}$) or a conical pore, with $R_{p,1} < R_{p,2}$, where $R_{p,1}$ and $R_{p,2}$ are the radii at the outer ends of the channel. The electrolyte concentrations are fixed at their bulk concentrations ($c_i = c_{i,0}$) at the extremities of the electrolyte compartments. These boundaries are positioned at 10 μm away from the nanoporous membrane. This is a realistic thickness for the diffusion boundary layer (DBL) in flow applications (especially when a spacer is used) and is sufficiently far away to ensure electroneutrality. An external electric field is applied over the membrane by setting the electrostatic potential at these far-end boundaries as $\phi = V_{applied}$ and $\phi_L = 0$. This model represents a case of an isolated membrane with liquid at either side (i.e., without electrodes in our domain), to deconvolute the effects of the membrane from electrode effects.

The non-solid boundaries orthogonal to the membrane surface (on the right side in Fig. 2b) are sufficiently far-away from the nanopore to prevent edge effects ($R_{total} \gg R_{pore}$), with R_{total} also serving as a lever to obtain desired membrane porosity. At these boundaries, zero charge is enforced ($\nabla\cdot\boldsymbol{D} = 0$, where $\boldsymbol{D}$ is the electric displacement field), and a no-flux boundary was also employed to ensure a constant DBL thickness. We stress that including modelling domains at both far ends of the nanopore (in our case 10 μm liquid), as well as next to the pore ($R_{total} \gg R_{pore}$), are essential to represent an array of nanopores. Single nanopores have obtained extremely low ionic resistance in literature [37–39], but are not representative for an array because of the absent porosity and diffusion boundary layers, which are intrinsic to larger samples with arrays of nanopores.

At the interface of the membrane surface and the electrolyte, a surface charge density (σ_S) is defined. Although many models use σ_S as a fitting parameter, this simplification can reduce the accuracy of the model since σ_S depends on the local electrolyte concentration and on also the pore size due to double layer overlap, which are parameters that may vary along the pore length. Therefore, we followed the work of Berg and Ladipo [40], who derived an analytical solution for the Poisson-Boltzmann equation and σ_S. They assumed that the surface charge density is entirely screened by counter-ions, which is a reasonable assumption for highly charged surfaces ($\phi_0 > \frac{e}{k_BT}$). In this way, the surface charge was defined as:

$$\sigma_S = \frac{4\frac{\varepsilon\varepsilon_0 k_B T}{eR_p}\left[1 - \exp\left(-\frac{e\phi_0}{2k_BT}\right)\right]}{2 - \exp\left(-\frac{e\phi_0}{2k_BT}\right)} \tag{5}$$

where ϕ_0 is the surface potential, for which we used the ζ-potential value for aluminum oxide in neutral solutions (~40 mV) [41,42]. By assuming the ζ-potential as the boundary potential, the modeled boundary is located at the shear plane and the model does not solve for the Stern layer. The underlying assumption is that no ion transport occurs through the Stern layer [43], which we assume to have a thickness of 0.5 nm and use a correction to the modeled pore size.

For the fluid flow, the outer ends of the electrolyte compartments are set at atmospheric pressure, thereby preventing pressure-driven flow through the nanopores. No-slip boundary conditions ($\boldsymbol{u} = 0$) and no-flux boundary conditions are employed for the fluid and species transport at the pore surface, since it is assumed to be impermeable ($-\mathbf{n}\cdot\mathbf{J}_i = 0$).

We varied the pore radii ($R_{p,1}$ and $R_{p,2}$), pore length (L_p), electrolyte

concentrations (C_{high} and C_{low}), surface potential (ϕ_0), and porosity. Pores smaller than 5 nm were not simulated because the continuum approach likely would not hold for lower values [22]. [43] The base conditions were with a pore size of 8 nm (7 nm effectively due to the Stern layer), a pore length of 1 μm, a surface potential of 40 mV, a porosity of 12 %, a DBL thickness of 10 μm, and either 50 mM KCl on both sides of the membrane or 10 mM on one side and 50 mM on the other side. The parameters were varied one at a time, keeping the remaining ones constant. The current-voltage data (minimum 15 points) was fit in MATLAB using a 3rd degree polynomial function, and its first derivative was taken as the ionic resistance.

3. Results and discussion

3.1. Axial profiles

To gain insight into the selectivity mechanism and the entrance effects, we simulated a pore with an 8 nm diameter and 50 nm length, with a 40 mV surface potential, between two compartments of 50 mM concentration, and plotted the concentration, potential and ion flux profiles along the pore length (Fig. 3). For clarity, Fig. 3a shows the cross-section of a nanopore, the normalized z/L_{pore} position, and the direction of the most significant migration and diffusion contributions of both ion species when a positive potential is applied across the anion-selective nanopore.

Fig. 3b shows a clear Donnan potential at the entrance and exit of the pore, and a corresponding abrupt increase in counter-ion concentration and decrease in co-ion concentration. This Donnan potential is responsible for the selectivity, which means that the pore entrances have a significant role [23]. Inside the pore, the concentration has a slight linear increase in the direction toward which Cl^- are migrating (more positive potentials).

Fig. 3c shows the flux contributions of diffusion and migration within the pore. It can be observed that the large potential gradients at the entrances of the pore shown in Fig. 3b, cause large migration peaks for both ions, which are largely compensated by diffusion in the opposite direction, as expected from the Donnan equilibrium. Within the pore however, mainly migration of Cl^- is observed which drives the selective ionic current through the pore.

Fig. S1 depicts another important transport mechanism in NFMs, which is surface conductance. Surface conductance is related to the higher concentration of ions close to the pore wall, where the fluid is both more conductive and more selective, due to the increased local charge. In other words, when a driving force is applied across the NFM, ion migration preferentially occurs close to the pore walls [44].

3.2. Effect of concentration

Fig. 4a shows the experimentally obtained ionic resistances for the 10 nm pore sized AAO membranes. Firstly, the observed values, especially at low concentrations, are significantly higher than expected based on the pore geometry and initial modeling results. This is caused by the low effective porosity of the commercial AAO membranes. In our previous work [27], we saw that the nanopores contract, widen and even diverge and converge within the first few tens of nm from the surface, which means that most pores do not connect the two sides of the membrane as we show in Fig. 1c. Fig. 4b shows the simulated ionic resistance where the porosity of the membrane was used as a fitting parameter. The obtained porosity was 0.09 %, and it can be observed that the data fits well with experimental data, except for the peak around 0 mA/cm^2. A similar simulation but for 12 % porosity (realistic value for AAO membranes) can be found in Fig. S2a. It shows that the ionic conductivity of these membranes can be improved by more than two orders of magnitude.

The experimentally obtained ionic resistances (Figs. 4a and 5a) show a peak in resistance at low current densities. This peak in resistance does

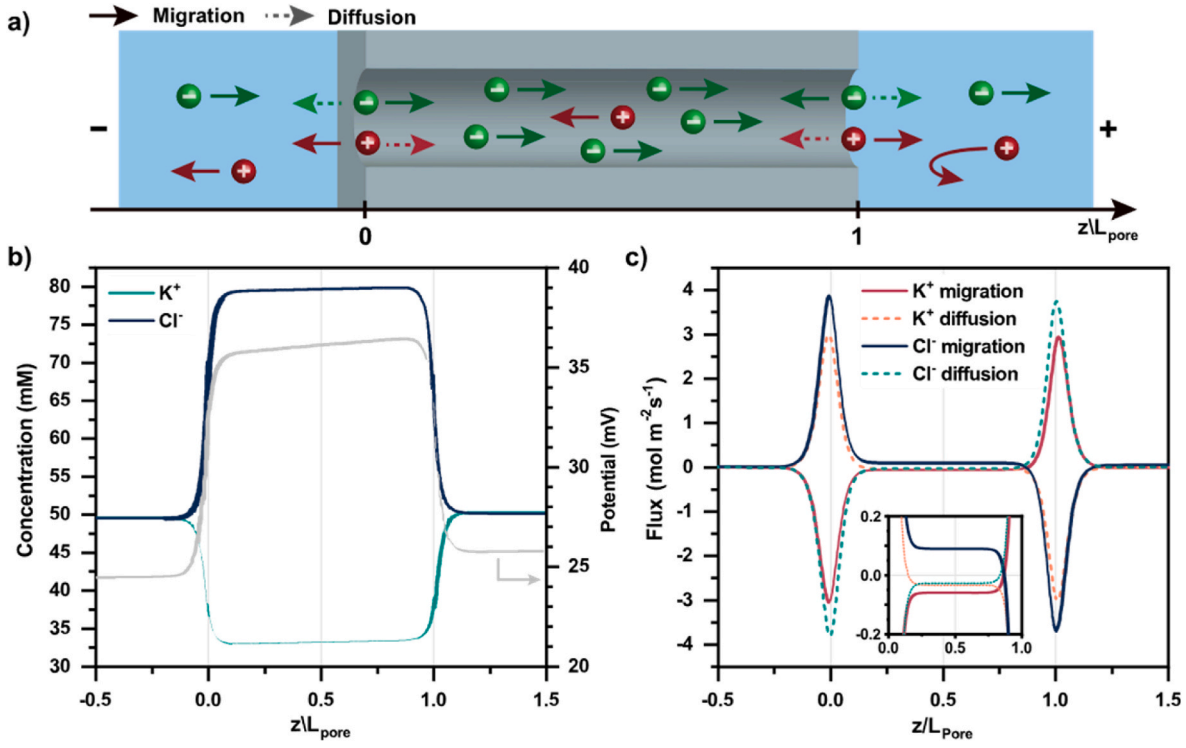

Fig. 3. – Simulations for an 8 nm in diameter and 50 nm in length pore with a 40 mV ζ-potential at 0.05 V applied potential. The pore was placed between two compartments with 50 mM solution. a) schematic illustration showing the anion-selective nanopore, the z/L_{pore} position and the direction of ion migration under positive potentials ($V_{applied}$), b) average concentration and potential (grey line, secondary axis) within the pore, and c) flux contributions of diffusion and migration in the z-direction for K^+ and Cl^- ions. The insert shows a zoom-in on the fluxes within the pore.

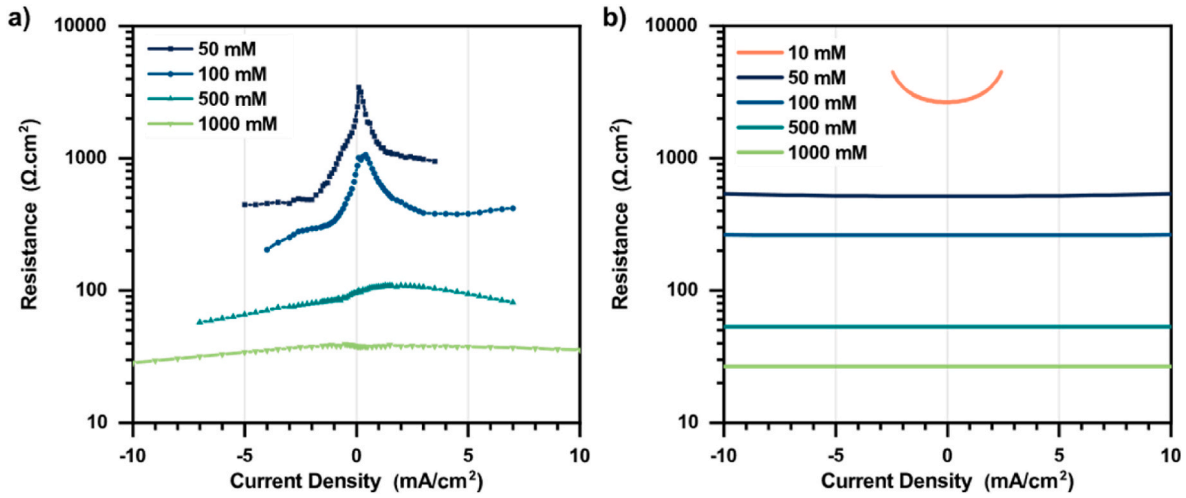

Fig. 4. – a) Ionic resistance of 10 nm pore sized AAO membranes when placed between two compartments with the same concentration on both sides. b) Simulated ionic resistance for a nanopore with a 10 nm pore size, 50 μm in length, 40 mV of surface potential, with porosity as a fitting parameter (0.09 %).

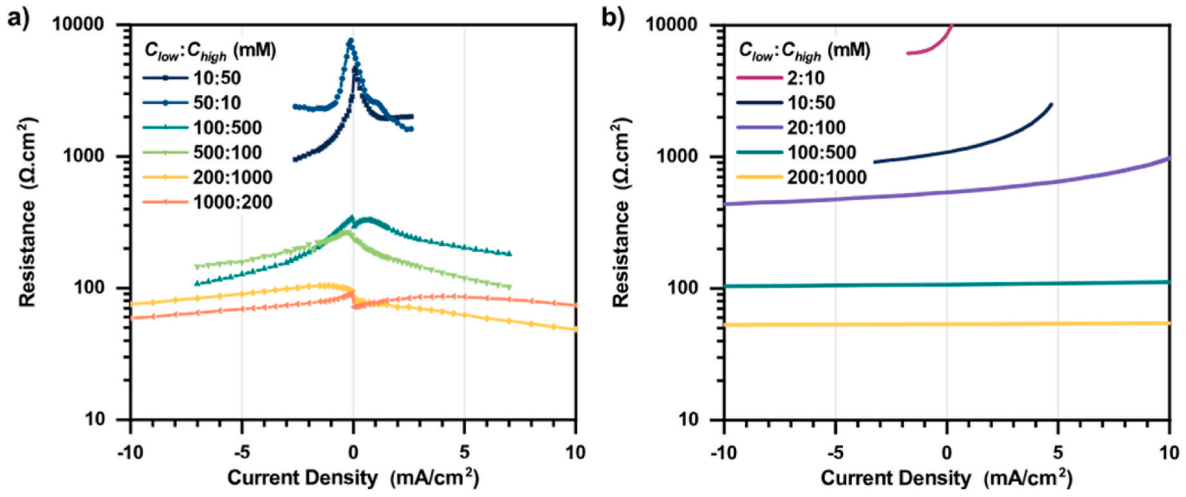

Fig. 5. a) Ionic Resistance of 10 nm pore sized AAO membranes when placed between two compartments with different concentrations the two sides, a C_{high}:C_{low} ratio of 5. The membranes were also inverted to account for non-idealities in the pore geometry. b) Simulated ionic resistance, with porosity as a fitting parameter.

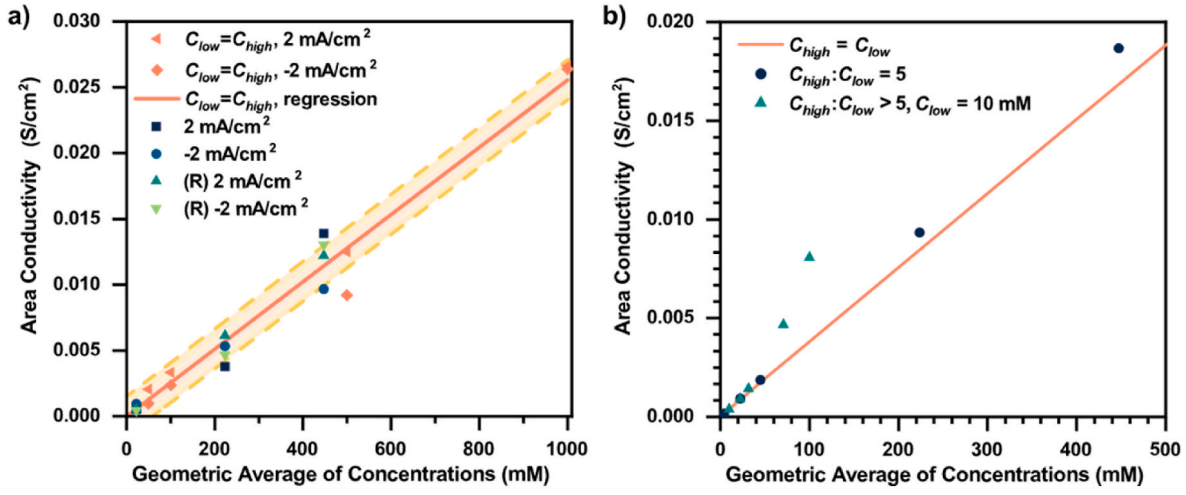

Fig. 6. Area conductivity vs geometric average of concentrations C_{high} and C_{low}. The linear fit of the data pertaining to $C_{high} = C_{low}$ is displayed as a line, with the respective standard error as a dashed line, and the symbols represent the data relating to experiments with $C_{high} \neq C_{low}$. A) experimental results, where C_{high}:$C_{low} = 5$ b) simulations. Note that the figures do not have the same scales.

not seem to be solely explained by the current density, since the peak is shifted to about 2 mA/cm^2 for the 500 mM case. Rather, the peak in resistance is observed when the membrane voltage is approximately 0.2 V (Table S1). To our knowledge, this has not been observed in the literature, and it is not captured by analytical/numerical models. While we are not certain why this peak occurs, it could be related to the voltage contribution of the ζ-potential of the material, which is more significant at lower potentials. Even though the potential over the membrane is a floating potential that should not alter the membrane charge, it is remarkable that the electrolyte potential affects the resistance. Alternatively, it could be related to electric-field induced changes to the ζ-potential and electro-osmotic flows [45]. In the field of nanofluidics, similar nanochannels are often used at very low ionic currents [46,47]. If this effect extends to other nanochannel systems, it could be causing an under-estimation of the conductivity of the nanochannels for larger-scale applications.

Perhaps the most important observation from Fig. 4 is the linear relationship between conductivity and electrolyte concentration (plotted in Fig. 6). This is unlike polymeric ion-exchange membranes where the measured conductivity plateaus after ~0.3 M of external electrolyte concentration. Ion transport in polymeric IEMs occurs through microcavities and microchannels in series (Fig. 1a) [48], where conductivity in the microchannels is determined by the counter-ions, which have a fixed concentration. Meanwhile, in NFMs, the surface charge density, and thus the membrane conductivity, is affected by the local electrolyte concentration within the pores. Therefore, the conductivity of NFMs increases with increasing reservoir concentration, without a plateau. However, the ion selectivity reduces at higher concentrations [27].

In more detail, the simulations shown in Fig. 4b demonstrate a higher resistance at higher current density, especially at low concentrations, which indicates a substantial impact of concentration polarization. Fig. S3a shows the concentration profiles of the entire geometry, at 5 mM bulk electrolyte and large applied voltages. The figure demonstrates that on the depleting side, the electrolyte concentration is significantly reduced close to the membrane surface, which is the cause for the observed limiting current density. Similar limiting currents are observed in polymeric IEMs [49,50]. Such effects are difficult to observe in the experimental results due to the limited current densities we can reach experimentally at low electrolyte concentrations.

In practical conditions (e.g. in electrodialysis and reverse electrodialysis), the concentration may differ at either side of the membrane. Previous work showed that the resistance of polymeric membranes is dependent on both concentrations, more dominantly on the lower concentration [48]. Moreover, as we know that the AAO membrane is asymmetric, we additionally add the direction of the concentration gradient as a parameter to study for nanofluidic ion-exchange membranes. Fig. 5a and b shows the experimental and simulation results of placing an AAO membrane between two compartments with different concentrations – in this case, the higher concentration side (C_{high}), is 5 times more concentrated than the lower concentration (C_{low}).

The results for distinct concentrations (Fig. 5) indeed shows asymmetric resistance plots. When the counter-ions migrate against the concentration gradient (i.e., for C_{low}:$C_{high} > 1$ at positive current density), the resistance is higher than when the current or concentration gradient is reversed. Although the concentration gradient itself plays a role, this is mostly a consequence of concentration polarization. The concentration profiles in Fig. S3b show that the concentration on the C_{low} side is close to 0 at the highest applied voltage. At high concentrations, the concentration gradient is larger in magnitude, but the resistance has a less pronounced increase – this is mostly because concentration polarization is less pronounced at high concentrations, but also because the NFM is less selective, allowing both ion species to migrate across further reducing concentration polarization. Concentration polarization can be reduced for example by increased mixing of the electrolyte, which reduces the diffusion boundary layer thickness.

Fig. 5a provides further evidence that the commercial AAO membranes do not have perfectly symmetrical channels. For each concentration, when the concentration gradient was inverted, the resulting resistance (and in particular the peak) differs depending on the orientation. This is evidence for asymmetry, such as conicity of the nanopores [51].

Larger C_{high}:C_{low} ratios were also simulated. Fig. S4a shows the result of a simulation with a fixed C_{low} at 10 mM and increasing C_{high}. The figure shows an increased resistance at positive current densities, even at higher C_{high} concentrations. However, contrary to the previous scenario at low concentrations, C_{low} doesn't deplete – the concentration on the C_{low} side actually increases closer to the NFM (Fig. S4b). In this case, the resistance is only increased because counterion migration occurs in opposite direction of the concentration gradient.

When the concentration is different on the two sides of the membrane, the question arises, which concentration, C_{high} or C_{low}, drives the conductivity? By taking the values at 2 mA/cm^2 and -2 mA/cm^2 from Figs. 4a and 5a, we plotted the area conductivity against concentration (Fig. 6a). The data relating to the experiments with equal concentrations on both sides of the membrane fits into a linear relationship. Interestingly, when taking the data where the concentrations on the two sides differ, it reasonably fits the same linear relationship only when plotted against the geometric average of the concentrations - shown with individual points in Fig. 6a. Fig. S5 shows that the same conductivity data plotted against the arithmetic average or the harmonic average of the concentrations do not fit the linear relationship established by the $C_{high} = C_{low}$ experiments.

To further understand the effect of different concentrations on the membrane resistance, Fig. 6b shows the same analysis for the simulation results (from Figs. 4b and 5b and S4a). This analysis shows that there is a good agreement between the $C_{high} = C_{low}$ line and the geometric average of the concentrations at low concentration ratios, but the fit deviates when the ratio between C_{high} and C_{low} is very high. Nevertheless, these results indicate that once the relationship between conductivity and concentration is known, the geometric average of C_{high} and C_{low} can be used to estimate the conductivity for when the NFM is placed between two different electrolyte concentrations. Moreover, in our previous work [27], we found that the selectivity is also governed by the geometric average of the concentrations on both sides.

3.3. Effect of pore size and shape

We further studied the impact of pore size on membrane resistance. Fig. 7a shows the resistance of AAO membranes with different pore sizes against current density. Other pore sizes also show the same peak in resistance close to 0 mA/cm^2 as observed with the 10 nm AAO membrane. The discontinuity for the 3/150 nm membrane is unclear, but this could be an artifact due to the order of measurements (i.e., hysteresis from previous potential due to capacitance). All the nearly-symmetric pores (10, 20, 50 nm) have similar conductivities – the observed differences in resistance are more likely to stem from differences in porosity, ageing and the slight asymmetry of the AAO. Therefore, it can be stated that for cylindrical nanopores the pore size does not have a notable impact on conductivity. This is consistent with the results of our simulations (Fig. 7b and c) and implies that the ion mobility within the nanopores is not significantly affected by the increased confinement in smaller nanopores. The simulations in Fig. 7c also show that cylindrical pores with a smaller diameter (<8 nm) are more conductive, due to the higher average electrolyte concentration in small charged channels. On the other hand, the model does not consider a varying diffusion coefficient within the nanopore in the radial direction, which has been shown to decrease within the electrical double layer [52]. Not accounting for the decrease in diffusivity in the diffuse layer could result in a small overprediction of the conductance, but this would in part be compensated by the stagnant Stern layer in our model, whereas molecular simulations indicate that ion mobilities are small but finite in the Stern

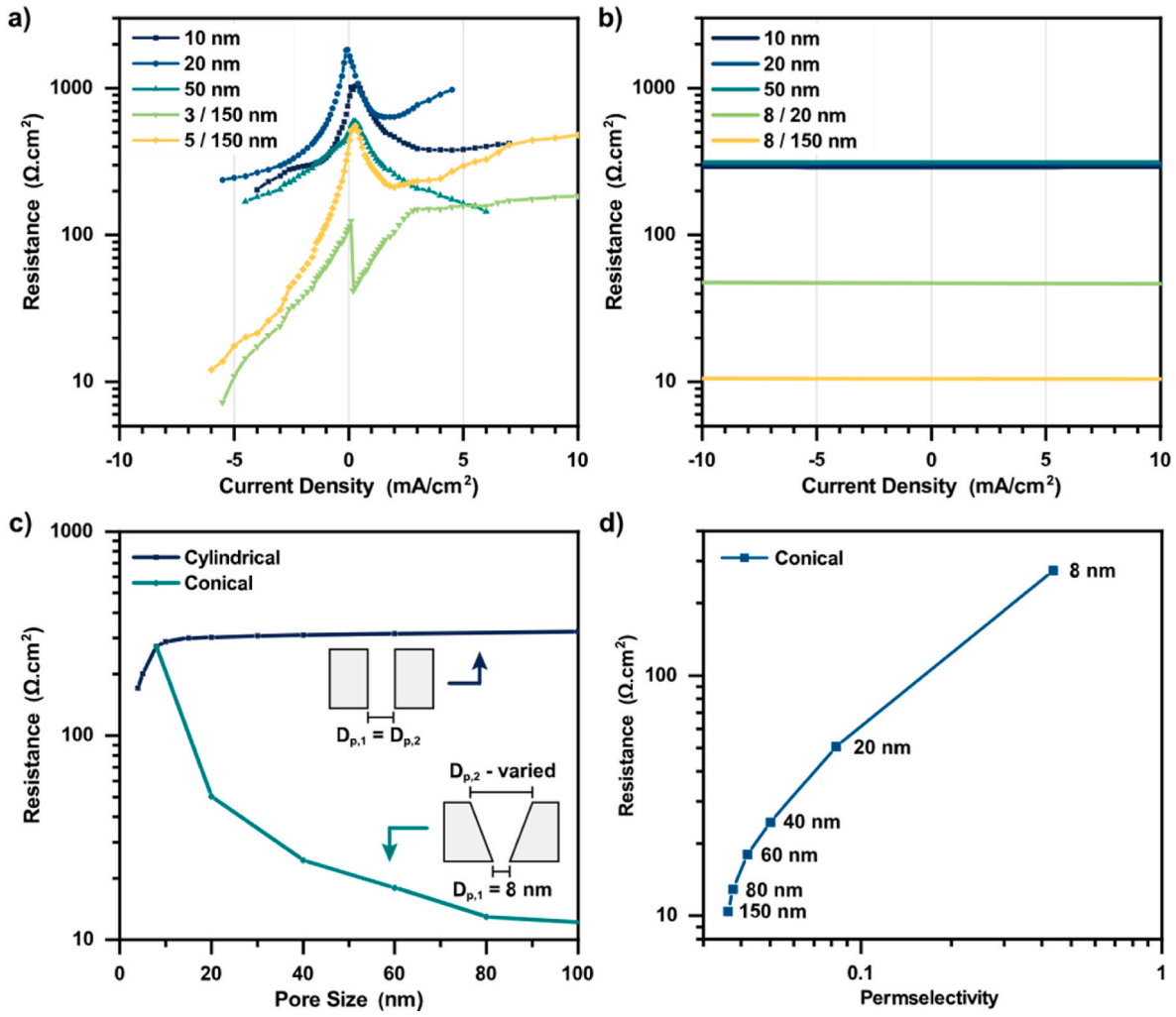

Fig. 7. – a) Membranes with different pore sizes – two asymmetric membranes with a thin selective layer and a support layer with 150 nm pore size, and three membranes with uniform pore sizes (10, 20 and 50 nm), placed between two compartments with 0.1 M KCl. b) Simulated ionic resistance for three cylindrical nanochannels (10, 20 and 50 nm) and two conical nanochannels with 8 nm as the smaller diameter, and 20 and 150 nm at the larger side. c) comparison of the ionic resistance of conical and cylindrical channels when varying the pore size, at −5 mA/cm^2. Only the larger pore size ($D_{p,2}$) was varied in conical nanopores, while keeping the smaller one ($D_{p,1}$) at 8 nm. d) Ionic resistance plotted against the permselectivity (at −5 mA/cm^2) of conical nanopores. $D_{p,2}$ is indicated on the figure for each point.

layer [45,53]. The effect of these modeling choices on the result can become more significant as the pore radius decreases.

The asymmetric channels with 3 and 5 nm pore sizes (Fig. 7a) show an increased conductivity in one direction. A lower resistance is observed when a negative current is applied, which corresponds to when the anions first enter the large pore size and then reach the selective layer. When this is the case, the area resistance drops below 10 Ω cm^2, which means that their conductivity is even comparable to polymeric IEMs. In our previous work [27], we have shown that this pore geometry was not able to ensure sufficient permselectivity because the narrow part is too short (few nanometers) to create charge selectivity. However, the enormous decrease in membrane resistance suggests that the pore geometry is an important lever, and probably asymmetric pores with a somewhat longer neck could be useful to balance a good conductivity and selectivity of NFMs.

Therefore, we simulated conical nanopores, while keeping in mind the manufacturing possibilities and methodology. In practice, to create conical nanopores AAO membranes are anodized multiple times to create a larger pore size variation along the membrane thickness, e.g. for the fabrication of nanoneedles. Therefore, we used a fixed pore diameter of 8 nm at the lower pore size ($D_{p,1}$), and progressively increased the larger pore size, without changing the size of the geometry (which means that the porosity also increases with increasing $D_{p,2}$).

Fig. 7c shows the resistance of both cylindrical and conical nanopores with the varying pore size. In the case of conical nanopores, the smaller pore size was kept constant at 8 nm and the larger pore size was increased. The figure shows that the resistance significantly decreases with an increasing pore size, and therefore also porosity.

However, our simulation did not fully produce the expected results for conical nanopores – this pore geometry typically induces the current rectification effect [44,51], which was not the case in our simulation. In Fig. 7b, for the conical nanopores, a lower resistance should have been observed at negative current than at positive ones. At positive currents, the resistance was expected to be closer to the resistance of cylindrical nanopores, because of the entrance effects [54]. On the other hand, we did observe a “rectified” ion transport, with higher transport numbers at negative currents (Fig. S6a). This effect was especially pronounced at low concentrations, because of the increased selectivity.

The increased conductivity of conical nanopores comes at a price: an equal decrease is observed in the permselectivity (Fig. 7d). Despite surface conductance, the selectivity of the NFMs largely stems from the entrance effects. Therefore, when ions enter the membrane through the

larger pore size, where the selectivity is significantly decreased, the total membrane selectivity is compromised. Fig. S6b shows the concentration and potential profiles for the conical nanopores, and there is a notable absence of a Donnan potential on the large pore size side. This decrease in selectivity could be mitigated by not only making the base diameter (i.e., side with largest opening) larger, but also reducing the tip diameter. Experimental work has revealed that conical nanopores could achieve higher conductivity and selectivity for counter-/counter-ion transport [55]. Also the cone angle (and thus the length of the pore) impacts the Donnan exclusion and conductivity [56]. Hence, the additional freedom of conical nanopores provides more room for optimization to improve the selectivity – conductivity trade-off.

To give a start to this nanopore optimization, we simulate parameter values that could not be experimentally verified, but whose optimization could aid in the manufacturing of a conductive NFM, without the loss of selectivity. Fig. 8 present the effects of porosity, pore length (for a straight nanopore) and surface potential, to predict the possibilities of NFMs with optimal performance.

3.4. Effects of porosity, pore length and surface potential

Fig. 8a shows the effect of porosity, which is as expected – the resistance increases with the decrease in porosity, or in other words, the conductivity increases linearly with the increase in porosity. The deviation from linearity observed at higher porosities is caused by concentration polarization and fluid velocity differences close to the pore entrance. When an NFM has a higher pore density, a higher current can be achieved, and naturally the concentration polarization will be more significant. However, this result also indicates that the concentration polarization must be considered when going to high pore densities and high currents densities.

Since resistance and selectivity of the membrane both scale with its thickness, the pore length is an important parameter to optimize. Fig. 8b shows the effect of pore length on resistance. Although it is not as pronounced as the effect of concentration, we observe a linear relationship between resistance and pore length past 1 μm. Increasing the length up to 1 μm, does not show a dramatic increase in resistance. At lower pore lengths, the concentration gradient within the channel plays a role - although the resistance is proportional to the length, the decrease in concentration gradient in longer nanochannels reduces back diffusion and makes the ion transport more efficient. Our previous work showed that increasing the pore length from a couple of tens of nanometers to a couple of hundreds of nanometers greatly improved the selectivity, but increasing it beyond an a couple of micrometers doesn't further affect the selectivity significantly (shown in Fig. 8b, secondary axis) [27]. Considering the trade-off between conductivity and selectivity, the optimum pore length likely lies in the 0.5–5 μm range, depending on the application and remaining membrane and fluid properties.

The surface potential shown in Fig. 8c, has an almost negligible effect on conductivity, which can be counter intuitive. A larger surface potential increases the surface charge density and therefore the fluid charge inside the nanopore, which has a major impact on selectivity. However, despite the larger charge separation, the total concentration of charge carriers inside the nanopore does not significantly increase, thus the conductivity remains almost unaffected by the magnitude of the surface potential. Additionally, surface charge density reaches a plateau at surface potentials close to 100 mV (Equation (5)).

Galama et al. [48] have shown that when a polymeric IEM is placed between two solutions of different concentrations, it is the lower concentration side that determines the conductivity, due to the influence of (electro)osmotic flows on the concentration profile inside the membrane. In this work, we have shown that for NFMs, it is the geometric average of the concentrations that dictates the conductivity, and not C_{low}. Therefore, (electro)osmosis certainly plays a different role on the concentration profiles inside NFMs. According to our model and other models in literature [23], the concentration changes linearly along the length of the NFM, a very different concentration profile than those observed in polymeric IEMs. Moreover, in polymeric IEMs, ions typically lose part of their hydration shell upon entering the polymeric structure [57]. In NFMs, since the pore size is larger, and no interactions with fixed charged groups take place, it is likely that ions will predominantly remain hydrated. Additionally, since electroosmotic mobility can be reduced within the electrical double layer relative to bulk electrolyte [58], we expect that due to the larger pore size of NFMs, electroosmosis will be larger than in polymeric IEMs. Electroosmosis can have positive effects on the conductivity, since it can reduce concentration polarization, and enhance ionic transport. On the other hand, for applications, such as electrodialysis, where the objective is to obtain a concentrated stream, a larger water transport due to electroosmosis will limit the achievable concentration in the stream.

In this work, we have shown that electrolyte concentration is the main driver for NFM conductivity. However, at high electrolyte concentrations NFMs also lose selectivity, which means that optimizing their performance is hindered by a similar conductance-selectivity trade-off as in polymeric IEMs. Nevertheless, they can potentially outperform polymeric IEMs in specific applications. An example of such an application is power generation through RED, where the membrane is placed between a concentrated salt stream and a pure water or river water stream. This particular combination allows the membrane to be both selective and sufficiently conductive. Using our model, we simulated a nanochannel of 1 μm in length, 5 nm in pore size and 40 mV of ζ-potential, between two concentrations of 17 mM and 600 mM (river and sea water), and the resulting area resistance was found to be 0.11 Ω cm^2 (at −100 mA/cm^2). This is lower than most of the currently used polymeric IEMs, and previous work has shown that such a channel can also surpass them in terms of selectivity. Additionally, NFMs also offer

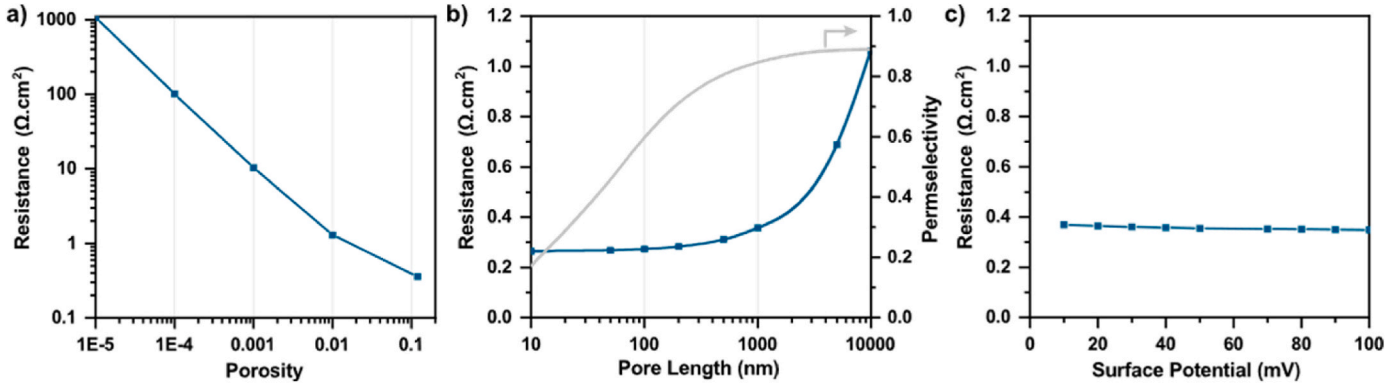

Fig. 8. – A pore of 1 μm length, 12 % porosity 3.5 nm pore size, and with a 40 mV zeta potential was simulated between two compartments of 50 mM KCl. The figure shows the result of varying a) porosity, b) pore length and c) surface potential.

the possibility of custom-tailored pore sizes and surface chemistries which is a promising avenue for specific functionalities, such as lithium extraction and separation.

Since conductivity is dependent on electrolyte concentration, standard NFMs are mostly not suitable for applications that require dilute solutions on both sides of the membrane. For such applications, the background conductivity of fixed charges is required for an energy efficient process. We believe that strategies that combine the benefits of polymeric IEMs and NFMs – oriented nanochannels which promote transmembrane transport surrounded by fixed charges, hold promise to significantly improve IEM conductivity. Such strategies include: the orientation of polymeric chains with fixed charges during polymerization to create ionic pathways in between, e.g. by an external electric field [59,60], or by controlling the hydrophobicity of the polymeric backbone and hydrophilicity of the functional groups [61,62]; using metal-organic frameworks or covalent-organic frameworks with charged functional groups and defined nanochannels [63,64], or functionalizing inorganic material-based NFMs [65,66].

4. Conclusions

We have studied experimentally and numerically the conductivity of AAO membranes with different pore sizes, under different operational conditions such as current density and electrolyte concentrations. Experimentally, we observed that the conductivity is affected by membrane voltage with the lowest conductivity found close to 0.2 V. When using cylindrical nanopores, no significant effect of pore size on conductivity was observed, both in the experiments and simulations. However, using conical nanopores significantly improves the conductivity, although it is at the expense of selectivity, which is largely determined by entrance effects (when ions enter through a large pore entrance, the selectivity is compromised).

The pore length, or membrane thickness, is also a sensitive parameter – we estimate that the optimal value, considering the trade-off with selectivity lies in the 0.5–5 μm range, depending on the application. Surprisingly, the surface potential of the material has a low impact on conductivity. Although a membrane with a higher surface potential ensures better selectivity and charge separation within the fluid, our simulations show that since the total concentration of charge carries doesn't change; the conductivity is not affected.

The membrane conductivity is dictated by the bulk electrolyte concentration, with a linear relationship even up to 1 M. When the NFM separates two compartments of different electrolyte concentrations, the geometric average of the concentrations determines the conductivity. Therefore, NFMs are suitable for applications such as RED, where a dilute solution and a highly concentrated solution are used on either side – this ensures both their selectivity and conductivity. However, since NFMs do not have the background conductivity of fixed charges, they may not be suitable for applications where low electrolyte concentrations are used.

CRediT authorship contribution statement

Kostadin V. Petrov: Writing – original draft, Visualization, Methodology, Investigation, Formal analysis, Data curation, Conceptualization. **Jan-Willem Hurkmans:** Writing – review & editing, Software, Formal analysis. **Remco Hartkamp:** Writing – review & editing, Investigation, Formal analysis. **David A. Vermaas:** Writing – review & editing, Supervision, Funding acquisition, Conceptualization.

Declaration of competing interest

The authors declare that they have no known competing financial interests or personal relationships that could have appeared to influence the work reported in this paper.

Data availability

The data is available at the Zenodo platform via DOI 10.5281/zenodo.10716237

Acknowledgements

This work is part of the research programme Towards large-scale electroconversion systems (TOeLS) financed by Shell and the Top-sectors Chemistry, HTSM and Energy.

Appendix A. Supplementary data

Supplementary data to this article can be found online at https://doi.org/10.1016/j.memsci.2024.123238.

References

[1] J.R. Varcoe, et al., Anion-exchange membranes in electrochemical energy systems, Energy Environ. Sci. 7 (2014) 3135–3191.
[2] R. Xia, S. Overa, F. Jiao, Emerging electrochemical processes to decarbonize the chemical industry, JACS Au 2 (2022) 1054–1070.
[3] R. Sharifian, R.M. Wagterveld, I.A. Digdaya, C. Xiang, D.A. Vermaas, Electrochemical carbon dioxide capture to close the carbon cycle, Energy Environ. Sci. 14 (2021) 781–814.
[4] S. Lakshmanan, T. Murugesan, The chlor-alkali process: work in Progress, Clean Technol. Environ. Policy 16 (2014) 225–234.
[5] K. Jiao, et al., Designing the next generation of proton-exchange membrane fuel cells, Nature 595 (2021) 361–369.
[6] H. Strathmann, Electrodialysis, a mature technology with a multitude of new applications, Desalination 264 (2010) 268–288.
[7] B. Schwenzer, et al., Membrane development for vanadium redox flow batteries, ChemSusChem 4 (2011) 1388–1406.
[8] T. Sata, G.N. Jones, Ion Exchange Membranes, The Royal Society of Chemistry, 2004, https://doi.org/10.1039/9781847551177.
[9] Y. Tanaka, Ion Exchange Membranes Fundamentals and Applications, Elsevier Science, 2015, https://doi.org/10.1016/C2013-0-12870-X.
[10] H.B. Park, J. Kamcev, L.M. Robeson, M. Elimelech, B.D. Freeman, Maximizing the right stuff: the trade-off between membrane permeability and selectivity, Science 356 (2017) eaab0530.
[11] C. Espinoza, D. Kitto, J. Kamcev, Counter-ion conductivity and selectivity trade-off for commercial ion-exchange membranes at high salinities, ACS Appl. Polym. Mater. 5 (2023) 10324–10333.
[12] D. Kitto, J. Kamcev, The need for ion-exchange membranes with high charge densities, J. Membr. Sci. 677 (2023) 121608.
[13] Z. Zhang, L. Wen, L. Jiang, Nanofluidics for osmotic energy conversion, Nat. Rev. Mater. 6 (2021) 622–639.
[14] J. Kamcev, D.R. Paul, G.S. Manning, B.D. Freeman, Predicting salt permeability coefficients in highly swollen, highly charged ion exchange membranes, ACS Appl. Mater. Interfaces 9 (2017) 4044–4056.
[15] V.S. Nichka, et al., Modified microheterogeneous model for describing electrical conductivity of membranes in dilute electrolyte solutions, Membranes and Membrane Technologies 1 (2019) 190–199.
[16] A. Daniilidis, D.A. Vermaas, R. Herber, K. Nijmeijer, Experimentally obtainable energy from mixing river water, seawater or brines with reverse electrodialysis, Renew. Energy 64 (2014) 123–131.
[17] M.N.Z. Abidin, M.M. Nasef, J. Veerman, Towards the development of new generation of ion exchange membranes for reverse electrodialysis: a review, Desalination 537 (2022) 115854.
[18] C.A. Machado, et al., Redox flow battery membranes: improving battery performance by leveraging structure–property relationships, ACS Energy Lett. 6 (2021) 158–176.
[19] L. Gubler, Membranes and separators for redox flow batteries, Curr. Opin. Electrochem. 18 (2019) 31–36.
[20] D.A. Salvatore, et al., Designing anion exchange membranes for CO2 electrolysers, Nat. Energy 6 (2021) 339–348.
[21] Nanofluidics is on the rise, Nat. Mater. 19 (2020) 253.
[22] L. Bocquet, E. Charlaix, Nanofluidics, from bulk to interfaces, Chem. Soc. Rev. 39 (2010) 1073–1095.
[23] I.I. Ryzhkov, D.V. Lebedev, V.S. Solodovnichenko, A.V. Minakov, M.M. Simunin, On the origin of membrane potential in membranes with polarizable nanopores, J. Membr. Sci. 549 (2018) 616–630.
[24] T. Xu, et al., Advances in synthesis and applications of boron nitride nanotubes: a review, Chem. Eng. J. 431 (2022) 134118.
[25] R.C. Rollings, A.T. Kuan, J.A. Golovchenko, Ion selectivity of graphene nanopores, Nat. Commun. 7 (2016) 11408.
[26] Z. Zhang, L. Wen, L. Jiang, Nanofluidics for osmotic energy conversion, Nat. Rev. Mater. 6 (2021) 622–639.
[27] K.V. Petrov, M. Mao, A. Santoso, I.I. Ryzhkov, D.A. Vermaas, Design criteria for selective nanofluidic ion-exchange membranes, J. Membr. Sci. 688 (2023) 122156.

[28] M. Nishizawa, V.P. Menon, C.R. Martin, Metal nanotubule membranes with electrochemically switchable ion-transport selectivity, Science 268 (1979) (1995) 700–702.
[29] I. Vlassiouk, S. Smirnov, Z. Siwy, Ionic selectivity of single nanochannels, Nano Lett. 8 (2008) 1978–1985.
[30] A. Aixalà-Perelló, et al., Scalable and highly selective graphene-based ion-exchange membranes with tunable permselectivity, NPJ 2D Mater Appl 7 (2023) 46.
[31] J. Kim, S.J. Kim, D.-K. Kim, Energy harvesting from salinity gradient by reverse electrodialysis with anodic alumina nanopores, Energy 51 (2013) 413–421.
[32] Z. Ahmed, Y. Bu, L. Yobas, Conductance interplay in ion concentration polarization across 1D nanochannels: microchannel surface shunt and nanochannel conductance, Anal. Chem. 92 (2020) 1252–1259.
[33] W.J. Wruck, R.M. Machado, T.W. Chapman, Current interruption—instrumentation and applications, J. Electrochem. Soc. 134 (1987) 539.
[34] A.H. Galama, J.W. Post, H.V.M. Hamelers, V.V. Nikonenko, P.M. Biesheuvel, On the origin of the membrane potential arising across densely charged ion exchange membranes: how well does the teorell-meyer-sievers theory work? Journal of Membrane Science and Research 2 (2016) 128–140.
[35] H. Zhu, A. Ghoufi, A. Szymczyk, B. Balannec, D. Morineau, Anomalous dielectric behavior of nanoconfined electrolytic solutions, Phys. Rev. Lett. 109 (2012) 107801.
[36] E. Papadopoulou, J. Zavadlav, R. Podgornik, M. Praprotnik, P. Koumoutsakos, Tuning the dielectric response of water in nanoconfinement through surface wettability, ACS Nano 15 (2021) 20311–20318.
[37] A. Siria, et al., Giant osmotic energy conversion measured in a single transmembrane boron nitride nanotube, Nature 494 (2013) 455–458.
[38] D.V. Lebedev, et al., Ultra-low intensity light-driven ionic conductivity through a plasmonic nanopore, ACS Appl. Nano Mater. 7 (2024) 16172–16181.
[39] J. Feng, et al., Single-layer MoS2 nanopores as nanopower generators, Nature 536 (2016) 197–200.
[40] P. Berg, K. Ladipo, Exact solution of an electro-osmotic flow problem in a cylindrical channel of polymer electrolyte membranes, Proc. R. Soc. A 465 (2009) 2663–2679.
[41] J.L. Reyes Bahena, A. Robledo Cabrera, A. López Valdivieso, R. Herrera Urbina, Fluoride adsorption onto α-Al2O3 and its effect on the zeta potential at the alumina–aqueous electrolyte interface, Separ. Sci. Technol. 37 (2002) 1973–1987.
[42] S. Novak, M. Kalin, The effect of pH on the wear of water-lubricated alumina and zirconia ceramics, Tribol. Lett. 17 (2004) 727–732.
[43] R. Qiao, N.R. Aluru, Ion concentrations and velocity profiles in nanochannel electroosmotic flows, J. Chem. Phys. 118 (2003) 4692–4701.
[44] A.R. Poggioli, A. Siria, L. Bocquet, Beyond the tradeoff: dynamic selectivity in ionic transport and current rectification, J. Phys. Chem. B 123 (2019) 1171–1185.
[45] M.F. Döpke, F. van der Meij, B. Coasne, R. Hartkamp, Surface protolysis and its kinetics impact the electrical double layer, Phys. Rev. Lett. 128 (2022) 56001.
[46] L.-J. Cheng, L.J. Guo, Nanofluidic diodes, Chem. Soc. Rev. 39 (2010) 923–938.
[47] D.G. Haywood, A. Saha-Shah, L.A. Baker, S.C. Jacobson, Fundamental studies of nanofluidics: nanopores, nanochannels, and nanopipets, Anal. Chem. 87 (2015) 172–187.
[48] A.H. Galama, et al., Membrane resistance: the effect of salinity gradients over a cation exchange membrane, J. Membr. Sci. 467 (2014) 279–291.
[49] J.J. Krol, M. Wessling, H. Strathmann, Concentration polarization with monopolar ion exchange membranes: current–voltage curves and water dissociation, J. Membr. Sci. 162 (1999) 145–154.
[50] P. Długołęcki, B. Anet, S.J. Metz, K. Nijmeijer, M. Wessling, Transport limitations in ion exchange membranes at low salt concentrations, J. Membr. Sci. 346 (2010) 163–171.
[51] W.-J. Lan, et al., Voltage-rectified current and fluid flow in conical nanopores, Acc. Chem. Res. 49 (2016) 2605–2613.
[52] R. Hartkamp, B. Siboulet, J.-F. Dufrêche, B. Coasne, Ion-specific adsorption and electroosmosis in charged amorphous porous silica, Phys. Chem. Chem. Phys. 17 (2015) 24683–24695.
[53] M.F. Döpke, R. Hartkamp, The importance of specifically adsorbed ions for electrokinetic phenomena: bridging the gap between experiments and MD simulations, J. Chem. Phys. 154 (2021) 94701.
[54] M. Karimzadeh, Z. Seifollahi, M. Khatibi, S.N. Ashrafizadeh, Impacts of the shape of soft nanochannels on their ion selectivity and current rectification, Electrochim. Acta 399 (2021) 139376.
[55] M.A. Shehzad, et al., Biomimetic nanocones that enable high ion permselectivity, Angew. Chem. Int. Ed. 58 (2019) 12646–12654.
[56] Q. Liu, et al., Asymmetric properties of ion transport in a charged conical nanopore, Phys. Rev. E 75 (2007) 51201.
[57] R. Epsztein, E. Shaulsky, M. Qin, M. Elimelech, Activation behavior for ion permeation in ion-exchange membranes: role of ion dehydration in selective transport, J. Membr. Sci. 580 (2019) 316–326.
[58] D.G. Haywood, Z.D. Harms, S.C. Jacobson, Electroosmotic flow in nanofluidic channels, Anal. Chem. 86 (2014) 11174–11180.
[59] J.-Y. Lee, J.-H. Lee, S. Ryu, S.-H. Yun, S.-H. Moon, Electrically aligned ion channels in cation exchange membranes and their polarized conductivity, J. Membr. Sci. 478 (2015) 19–24.
[60] J. Hyun, et al., Magnetic field-induced through-plane alignment of the proton highway in a proton exchange membrane, ACS Appl. Energy Mater. 3 (2020) 4619–4628.
[61] X. Zhu, et al., Polymeric nano-blue-energy generator based on anion-selective ionomers with 3D pores and pH-driving gating, Adv. Energy Mater. 10 (2020) 2001552.
[62] X.-C. Chen, H. Zhang, S.-H. Liu, Y. Zhou, L. Jiang, Engineering polymeric nanofluidic membranes for efficient ionic transport: biomimetic design, material construction, and advanced functionalities, ACS Nano 16 (2022) 17613–17640.
[63] J. Lu, et al., Efficient metal ion sieving in rectifying subnanochannels enabled by metal–organic frameworks, Nat. Mater. 19 (2020) 767–774.
[64] J. Lu, H. Wang, Emerging porous framework material-based nanofluidic membranes toward ultimate ion separation, Matter 4 (2021) 2810–2830.
[65] W. Shi, et al., Functionalized anodic aluminum oxide (AAO) membranes for affinity protein separation, J. Membr. Sci. 325 (2008) 801–808.
[66] L. Xie, et al., Surface charge modification on 2D nanofluidic membrane for regulating ion transport, Adv. Funct. Mater. 33 (2023) 2208959.